

MIT Open Access Articles

DISCOVERY OF THE NEAR-INFRARED COUNTERPART TO THE LUMINOUS NEUTRON-STAR LOW-MASS X-RAY BINARY GX 3+1

The MIT Faculty has made this article openly available. *Please share* how this access benefits you. Your story matters.

Citation: Van den Berg, Maureen, Jeroen Homan, Joel K. Fridriksson, and Manuel Linares. "DISCOVERY OF THE NEAR-INFRARED COUNTERPART TO THE LUMINOUS NEUTRON-STAR LOW-MASS X-RAY BINARY GX 3+1." *The Astrophysical Journal* 793, no. 2 (September 16, 2014): 128. © 2014 American Astronomical Society.

As Published: <http://dx.doi.org/10.1088/0004-637X/793/2/128>

Publisher: Institute of Physics/American Astronomical Society

Persistent URL: <http://hdl.handle.net/1721.1/95419>

Version: Final published version: final published article, as it appeared in a journal, conference proceedings, or other formally published context

Terms of Use: Article is made available in accordance with the publisher's policy and may be subject to US copyright law. Please refer to the publisher's site for terms of use.



DISCOVERY OF THE NEAR-INFRARED COUNTERPART TO THE LUMINOUS NEUTRON-STAR LOW-MASS X-RAY BINARY GX 3+1*

MAUREEN VAN DEN BERG^{1,2}, JEROEN HOMAN³, JOEL K. FRIDRIKSSON¹, AND MANUEL LINARES^{4,5}

¹ Anton Pannekoek Institute for Astronomy, University of Amsterdam, Science Park 904, 1098 XH Amsterdam, The Netherlands; M.C.vandenBerg@uva.nl

² Harvard-Smithsonian Center for Astrophysics, 60 Garden Street, Cambridge, MA 02138, USA

³ Massachusetts Institute of Technology, Kavli Institute for Astrophysics and Space Research, 70 Vassar Street, Cambridge, MA 02139, USA

⁴ Instituto de Astrofísica de Canarias (IAC), Vía Láctea s/n, La Laguna, E-38205, S/C de Tenerife, Spain

⁵ Departamento de Astrofísica, Universidad de La Laguna, E-38206 La Laguna, Tenerife, Spain

Received 2014 June 7; accepted 2014 July 30; published 2014 September 16

ABSTRACT

Using the High Resolution Camera on board the *Chandra X-ray Observatory*, we have measured an accurate position for the bright persistent neutron star X-ray binary and atoll source GX 3+1. At a location that is consistent with this new position, we have discovered the near-infrared (NIR) counterpart to GX 3+1 in images taken with the PANIC and FourStar cameras on the Magellan Baade Telescope. The identification of this $K_s = 15.8 \pm 0.1$ mag star as the counterpart is based on the presence of a Br γ emission line in an NIR spectrum taken with the Folded-port InfraRed Echelette spectrograph on the Baade Telescope. The absolute magnitude derived from the best available distance estimate to GX 3+1 indicates that the mass donor in the system is not a late-type giant. We find that the NIR light in GX 3+1 is likely dominated by the contribution from a heated outer accretion disk. This is similar to what has been found for the NIR flux from the brighter class of Z sources, but unlike the behavior of atolls fainter ($L_X \approx 10^{36} - 10^{37}$ erg s⁻¹) than GX 3+1, where optically thin synchrotron emission from a jet probably dominates the NIR flux.

Key words: accretion, accretion disks – binaries: close – stars: individual (GX 3+1) – X-rays: binaries

Online-only material: color figures

1. INTRODUCTION

Low-mass X-ray binaries (LMXBs) are systems in which a neutron-star or black hole accretes matter from a low-mass secondary ($M \lesssim 1 M_\odot$). Most are only occasionally bright in X-rays, but some have been very X-ray luminous since their discovery. Neutron-star low-mass X-ray binaries (NS-LMXBs) with relatively weak magnetic fields show a wide variety of correlated spectral and variability behavior in X-rays. Based on this, two main subclasses are recognized (Hasinger & van der Klis 1989): the so-called Z sources, with luminosities close to or above the Eddington luminosity (L_{Edd}), and the atoll sources, with luminosities up to $\sim 0.5 L_{\text{Edd}}$; see Homan et al. (2010) for an overview.

To explain the high mass-accretion rates ($\sim 10^{-9} - 10^{-8} M_\odot \text{ yr}^{-1}$) that are implied by their X-ray luminosities, it has been suggested that the mass donors in the most luminous ($L_X \gtrsim 1 \times 10^{37}$ erg s⁻¹) NS-LMXBs are evolved stars (Webbink et al. 1983; Taam 1983). The evolutionary expansion of (sub-)giant companions can drive mass transfer rates in excess of those that occur in systems with main-sequence donors, where mass-transfer is driven by the loss of angular momentum. The evolutionary stage of the donor also affects the duration of the active X-ray–binary phase in the lifetime of an LMXB and might shape the LMXB X-ray luminosity function (XLF). Revnivtsev et al. (2011) suggested that the break around $\log L_X (\text{erg s}^{-1}) \approx 10^{37.3}$ in the LMXB XLF of our own Galaxy and nearby galaxies (Gilfanov 2004) separates systems with main-sequence companions from those with giant donors whose shorter active lifetimes would explain the steepening of the XLF. Their argument uses orbital period as a proxy of donor

size, and observations of a handful of systems confirm that this is a valid assumption in those cases. However, for about half of the sources with $L_X > 10^{37.3}$ erg s⁻¹ an orbital period or donor classification is not available.

Optical and near-infrared (OIR) studies can potentially clarify some of these issues. They shed light on the structure of the various accretion flow components, such as disks and jets (Russell et al. 2007) and can provide information on the binary parameters, such as orbital period and properties of the mass donor (e.g., Bandyopadhyay et al. 1999). Given that the population of bright NS-LMXBs is concentrated toward the heavily obscured Galactic bulge, the low extinction in the near-infrared (NIR)— $A_K \approx 0.1 A_V$ —makes it the preferred band to carry out such studies in that region.

With a luminosity of $(2-4) \times 10^{37}$ erg s⁻¹ (2–10 keV; den Hartog et al. 2003) GX 3+1 is one of the eleven most luminous and persistently bright Galactic NS-LMXBs. Ever since its discovery in 1964 (Bowyer et al. 1965) observations of GX 3+1 have found it to be a bright X-ray source. The detection of X-ray bursts (Makishima et al. 1983) indicates that it is a neutron star system. The best distance estimate of ~ 6.1 kpc is derived from the properties of a radius-expansion burst, assuming an Eddington limit that is appropriate for a hydrogen-poor atmosphere (Kuulkers & van der Klis 2000; den Hartog et al. 2003). The resulting maximum persistent bolometric luminosity is $\sim 6 \times 10^{37}$ erg s⁻¹ or $\sim 0.3 L_{\text{Edd}}$. Based on its spectral and variability properties, GX 3+1 is classified as an atoll source (Hasinger & van der Klis 1989). Similar to the bright atolls GX 9+1 and GX 9+9, GX 3+1 shows strong long-term X-ray flux modulations, which have a timescale of ~ 6 yr (Kotze & Charles 2010; Durant et al. 2010). Kotze & Charles (2010) suggested these modulations are the result of variations in the mass-transfer rate due to a solar-type magnetic-activity cycle in the donor star. However, since the long-term X-ray

* This paper includes data gathered with the 6.5 m Magellan Telescopes located at Las Campanas Observatory, Chile.

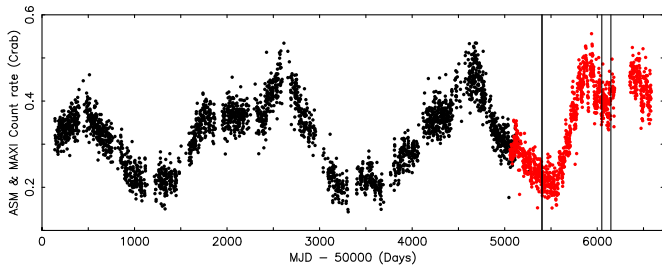


Figure 1. Long-term 2–10 keV *RXTE*/ASM (black points) and MAXI (red points) light curves of GX 3+1. Count rates were normalized to those of the Crab. Vertical lines indicate the times of our Magellan imaging observations. (A color version of this figure is available in the online journal.)

light curve of GX 3+1 covers only ~ 2.5 cycles of the brightness modulations, it is unclear if they are quasi-periodic or have a more random nature and are simply a manifestation of very-low-frequency noise. The lack of an accurate position for GX 3+1 has hampered the search for a counterpart, and thus far the orbital period of GX 3+1 remains unknown.

Naylor et al. (1991) were the first to look for an NIR counterpart to GX 3+1. They identified one candidate inside the region defined by the *Einstein* error circle and the lunar-occultation error box. More recently, Zolotukhin & Revnivtsev (2011) repeated the search using an additional position constraint imposed by a *Chandra* observation performed in continuous-clocking mode. In the highly elongated region of about $0'.5 \times 2''$, they identified two possible counterparts, viz. the one originally found by Naylor et al. (1991) and a much fainter source.

Here, we present the results of our own search for GX 3+1 in the NIR. Combining a newly determined accurate X-ray position with NIR imaging and spectroscopy, we have uncovered the true counterpart of GX 3+1 five decades after its discovery in X-rays. We describe the X-ray and NIR observations in Section 2, and the identification of the counterpart in Section 3. In Section 4, we discuss the origin of the NIR emission in GX 3+1, and make a comparison with other NS-LMXBs.

2. OBSERVATIONS AND DATA REDUCTION

2.1. X-Rays

2.1.1. *Chandra* HRC Observation

We observed GX 3+1 with the *Chandra* High Resolution Camera imaging detector (HRC-I; Zombeck et al. 1995) for 1.2 ks, starting on 2012 February 12 at 19:22:43 UTC. The High Energy Transmission Grating was inserted to lower the count rate and to limit distortions in the image that could adversely affect the image reconstruction. The data were analyzed using CIAO 4.5 (Fruscione et al. 2006). We ran the *wavdetect* tool on a 200×200 pixel image, centered on GX 3+1. This yielded the following source position (R.A., decl.): $17^{\text{h}}47^{\text{m}}56^{\text{s}}.077$, $-26^{\circ}33'49''.48$ (J2000); the formal *wavdetect* errors are negligible ($< 0''.01$ in each coordinate). About 2.1×10^4 photons were detected in a $2''$ radius circle centered around this position. No other X-ray sources were detected in the field, which made it impossible to improve the absolute astrometry of the image using X-ray sources with known accurate (radio or optical/NIR) counterpart positions. Therefore, the positional accuracy is limited by *Chandra*'s absolute astrometric calibration, which for the HRC-I is $\sim 0''.54$ (90% confidence).⁶

⁶ <http://cxc.cfa.harvard.edu/cal/ASPECT/celmon/>

Table 1
Magellan NIR Observations of the GX 3+1 Field

Epoch	Date (UT)	MJD ^a (UT)	Instrument	T_{exp} (s)	Seeing (")
1	2010 Jul 25	55402.0304	PANIC	540	1.1
2	2010 Jul 25	55402.9887	PANIC	540	0.6
3	2012 May 2	56049.3916	FourStar	594	0.4
4	2012 May 3	56050.3842	FIRE	571	0.6
5	2012 Aug 8	56147.1026	FourStar	705	1.1

Note. Modified Julian Date at the midpoint of the observation.

2.1.2. *RXTE*/ASM and MAXI Light Curves

We used public data from the All Sky Monitor (ASM) on board the *Rossi X-ray Timing Explorer* (*RXTE*; Levine et al. 1996) and from the *Monitor of All-sky X-ray Image* (MAXI) camera (Matsuoka et al. 2009) to construct a long-term 2–10 keV light curve of GX 3+1 from one-day average count rates (ctr). Data points with large uncertainties ($\text{ctr}/\sigma_{\text{ctr}} < 20$, with σ_{ctr} the standard deviation in ctr) were removed; for the MAXI data, we also removed a few-day-long flare around MJD 55916, whose origin and relation to GX 3+1 are unclear, and data between MJD 56187 and MJD 56351, which were affected by an outburst from a transient in the globular cluster Terzan 5. The count rates from both instruments were normalized to those of the Crab. The resulting light curve is shown in Figure 1. Strong long-term modulations with time-scales of several years are clearly visible. The vertical lines in Figure 1 indicate the times of our NIR imaging observations (see next section); the first two were only separated by about one day and appear as a single line.

2.2. Near-infrared

2.2.1. PANIC Imaging

A log of all our NIR observations is given in Table 1. We observed the field of GX 3+1 with the Persson's Auxiliary Nasmyth Infrared Camera (PANIC; Martini et al. 2004) on the 6.5 m Magellan Baade telescope in Las Campanas, Chile. Mounted on the Baade, PANIC's 1024×1024 pixel² HgCdTe detector has a $0'.127$ pixel⁻¹ plate scale, and a field of view of about $2' \times 2'$. Observations were obtained through the K_s filter (with a ~ 1.95 – 2.35 μm bandpass) on two consecutive nights, at the start and at the very end of 2010 July 25. On the first night, the seeing was poor at about $1''.1$, but this improved to $0''.6$ on the second night. We employed the same observing strategy on both nights. A nine-point dither pattern, with three 10 s exposures at each dither position, was repeated twice and resulted in a total exposure time of 540 s. Because the source density in the target field is very high, we also observed a relatively empty field centered on an interstellar dark cloud that is $50'$ away from GX 3+1. From these dithered offset sequences, taken immediately following the GX 3+1 observations, we constructed sky-background maps.

We used the PANIC data-reduction package written for IRAF to reduce the data. After dark-subtracting all science frames, the PANIC pipeline averages the exposures taken at each dither position and corrects for non-linearity of the detector response. Flat-fielding is achieved using master twilight flats. The processed offset-field exposures are median-combined to create an initial sky map. Objects detected in the sky-subtracted offset frames are masked out before doing a second iteration

of median combining, which creates the final sky map. The sky-subtracted GX 3+1 exposures are subsequently corrected for astrometric distortion and finally aligned and stacked into one master image for each night. We tied the astrometry of these master images to the International Celestial Reference System (ICRS) using about twenty unsaturated and relatively isolated Two Micron All Sky Survey (2MASS) stars in the field. Fitting for zero point, rotation angle, and scale factor gives an astrometric solution with an rms scatter of $\sim 0''.06$ in right ascension and declination; this is comparable to the intrinsic astrometric accuracy of 2MASS positions.

As a result of the poor seeing, the GX 3+1 images of epoch 1 were of little use to find, and determine the properties of, candidate NIR counterparts. Instrumental magnitudes for the image from epoch 2 were extracted with DAOPHOT point-spread-function (PSF) fitting photometry and are calibrated using the K_s magnitudes of eleven isolated and well-fitted 2MASS stars in the field. We derived a constant magnitude offset by averaging the differences between the instrumental and calibrated magnitudes of the comparison stars, which gives an rms scatter of 0.065 mag around the mean offset.

2.2.2. FourStar Imaging

On 2012 May 2 and August 8, we imaged the field of GX 3+1 in the K_s band with the FourStar camera (Monson et al. 2011) on the Magellan Baade telescope. The FourStar 2×2 array of 2048×2048 pixel² HAWAII-2RG detectors has a $0''.159$ pixel⁻¹ plate scale on the Baade and provides a full field of view of $10''.8 \times 10''.8$ with $19''$ wide gaps. We placed our target near the center of one of the four detectors. The seeing on May 2 was excellent ($\sim 0''.4$), but the poor seeing ($\sim 1''.1$) during the second run made the images collected on August 8 of little use for achieving our scientific goals.

On May 2, we employed a nine-point dither pattern with fifteen 4.4 s exposures at each dither position, for a total observing time of 594 s. Two sequences of an offset field bracketed the target observations. On August 8, we took one target and one offset sequence, each consisting of nine dithers with nine 8.7 s exposures at each position, for a total exposure of ~ 705 s. The data reduction steps are similar to those adopted for the PANIC images (Section 2.2.1), except that for the case of the FourStar images we used the SCAMP package (Bertin 2006) to correct for the geometric distortion. To this end, fifth-order polynomials were fitted to the cataloged and measured positions of 2MASS stars to map out the variable plate scale over the chip area. With the SWarp routines (Bertin et al. 2002) the images were resampled to distortion-corrected images with a linear plate scale of $0''.12$ pixel⁻¹, similar to the PANIC plate scale. The small degree of oversampling with respect to the intrinsic FourStar plate scale is justified by the non-integer dither offsets of the observing sequences. The astrometry of the final images was tied to the ICRS in the same way as we did for the PANIC images, which resulted in an astrometric solution with an rms scatter of $\sim 0''.065$ in right ascension and declination.

PSF photometry was performed on the final stacked image of epoch 3. The absolute calibration of the FourStar photometry was derived based on the calibrated PANIC photometry. We chose eleven isolated stars within $11''$ of GX 3+1 with a clean PSF measurement in the PANIC and FourStar images, and $14.3 < K_s < 16.0$ to derive the mean magnitude offset that converts FourStar instrumental to calibrated magnitudes. The rms scatter around this mean offset is 0.034 mag.

2.2.3. FIRE Spectroscopy

NIR spectra of two candidate counterparts (A 1 and A 2; see Section 3) were obtained with the Folded-port InfraRed Echelette (FIRE; Simcoe et al. 2013) spectrograph on the Magellan Baade telescope. FIRE is equipped with a 2048×2048 pixel² HAWAII-2RG HgCdTe detector. The spectrograph was used in the low-resolution longslit prism mode with a slit width of $0''.6$, yielding a continuous coverage of the 0.8 – 2.5 μm band and a resolving power in the K_s band of $R = 300$. In our setup, the spatial sampling across the slit is $0''.15$ per pixel.

Observations were taken on the night of 2012 May 3 starting at 09:02 UT when GX 3+1 was at an airmass of ~ 1.05 . The slit was positioned such that both candidate counterparts fell in the slit. Observing conditions were good with a typical seeing of $0''.6$; this is good enough to separate the PSF peaks of A 1 and A 2, which are only $\sim 0''.76$ apart. We executed a sequence of nine 63.4 s exposures and nodded the targets along the slit. The bright ($V = 8.3$) telluric standard HD 169291 of spectral type A0 V was observed after the GX 3+1 observations with a sequence of five one-second exposures.

We reduced the data mainly using IRAF routines. A master flat was created from two sets of dome flats, each optimized to have sufficient counts in either the blue or red part of the spectrum. Next, science exposures were subtracted in pairs; each frame was paired with the exposure nearest in time in which the stars were dithered to an offset position. This yields an initial sky subtraction, and enabled us to locate the stars in the slit. The resulting difference images were divided by the masterflat. In this crowded field, there are hardly any clean background patches to measure the residual sky. For this reason, we chose a few narrow background regions close to the targets, but especially in the H band (~ 1.5 – 1.8 μm), where the sky OH emission lines are strong, the signatures of an imperfect sky subtraction can be seen as sharp features in the final spectra, which add to the noise. We extracted the spectra by simply adding the sky-subtracted pixel values within the aperture limits. Given the small angular separation between the two targets, we defined a narrow, two-pixel wide extraction aperture to minimize the stars' mutual contamination, but as a result of our extraction method, it cannot be completely removed. The widely used optimal-extraction algorithm by Horne (1986) was developed for isolated stars, and indeed did not produce good results for the blended spatial profiles of our targets. The wavelength calibration was done using a neon-argon lamp exposure taken immediately following the GX 3+1 sequence. The errors in the dispersion solution are $\lesssim 0.001$ μm . Redward of 2.1 μm , there are only a few arc lines and a rapidly rising thermal background from the telescope; this makes the wavelength calibration very uncertain in that part of the spectrum. The individual spectra of each star were average-combined into a master spectrum after scaling the relatively featureless stretch of continuum between 2.1 and 2.15 μm to the same value. A master spectrum for the telluric standard was extracted in a similar way. We performed the telluric correction using the method and routines described in Vacca et al. (2003).

3. THE NIR COUNTERPART TO GX 3+1

Figure 2 shows the region around the new *Chandra* position of GX 3+1 in the K_s images from all four imaging epochs. The red circles represent the 90% confidence radius on the source position. These were computed by adding in quadrature the *Chandra* absolute pointing error ($0''.54$) and the errors in

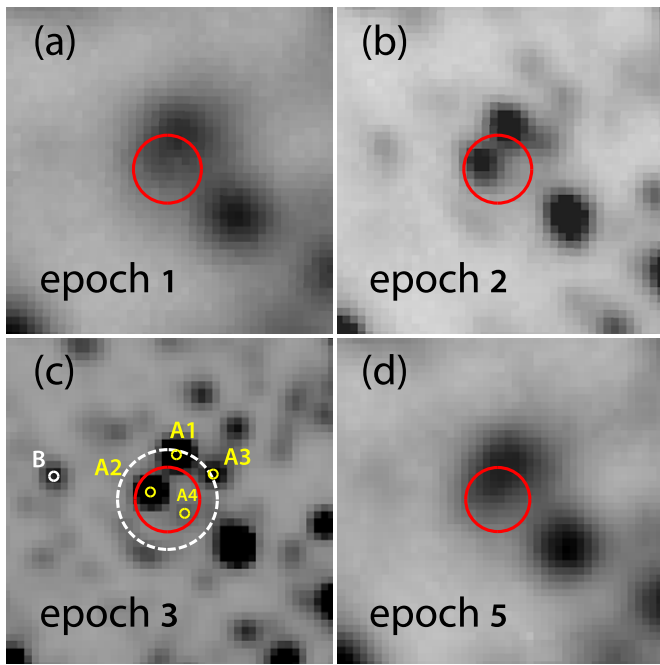


Figure 2. PANIC (top) and FourStar (bottom) images of all four imaging epochs centered on the new *Chandra* position of GX 3+1. The 90% confidence errors ($\sim 0''.58$) are indicated with red circles, whereas the 95% confidence error ($\sim 0''.83$) is shown as a white dashed circle in panel (c) only. Small yellow circles mark the positions of candidate NIR counterparts. Source B was considered to be a possible counterpart by Zolotukhin & Revnivtsev (2011) but this is ruled out by our new position. Each image is about $5''.5 \times 5''.5$ in size. North is up, east to the left.

(A color version of this figure is available in the online journal.)

the astrometric solutions of the PANIC and FourStar images (see Sections 2.2.1 and 2.2.2) scaled to 90% errors assuming a two-dimensional Gaussian distribution. For illustrative purposes, we also show the combined 95% error radius in Figure 2(c).⁷ From this figure, which shows the image taken under the best seeing conditions, it is clear that multiple K_s -band sources are viable counterparts to GX 3+1 based on their locations inside or very close to the 90% ($0''.58$ for this epoch) or 95% ($0''.83$) confidence radii; in principle, any of the sources marked with a small yellow circle could be the counterpart. Comparison of this image with

⁷ We note that the 95% confidence limit on the absolute pointing of the HRC-I is not known very accurately. We conservatively assumed $0''.8$; see the link in the previous footnote.

Table 2

Positions and Magnitudes of NIR Sources Near the New Position of GX 3+1

ID	α_{J2000}	δ_{J2000}	Δ ($''$)	$K_{s,epoch2}$	$K_{s,epoch3}$
A 1	17 ^h 47 ^m 56 ^s .063	-26°33'48".74	0.76	15.62 ± 0.01	15.62 ± 0.01
A 2	17 ^h 47 ^m 56 ^s .097	-26°33'49".35	0.31	15.82 ± 0.01	15.84 ± 0.01
A 3	17 ^h 47 ^m 56 ^s .015	-26°33'49".06	0.87	16.78 ± 0.02	16.84 ± 0.02
A 4	17 ^h 47 ^m 56 ^s .056	-26°33'49".71	0.37	18.12 ± 0.05	18.11 ± 0.04
B	17 ^h 47 ^m 56 ^s .214	-26°33'49".09	1.94	17.26 ± 0.02	17.13 ± 0.02

Notes. Δ is the offset between the positions of the NIR sources and the new *Chandra* position of GX 3+1. We consider A 2 to be the likely NIR counterpart to GX 3+1 based on the detection of a Br γ emission line in its K_s -band spectrum. The uncertainties in the magnitudes are the DAOPHOT errors on the PSF photometry. Additional errors in the photometric calibration with respect to 2MASS are <0.1 mag and are given in Sections 2.2.1 and 2.2.2.

the lower resolution UKIRT K image in Figure 5 of Zolotukhin & Revnivtsev (2011) shows that their candidate counterpart A is now resolved into four sources, which we label A 1 to A 4 in order of decreasing K_s brightness. Source B, the other counterpart proposed by Zolotukhin & Revnivtsev (2011), lies too far from the new *Chandra* position to still be considered a possible counterpart. Table 2 lists the coordinates of these stars together with their K_s magnitudes from epochs 2 and 3, during which they are detected without significantly suffering from blending.

The two candidate counterparts for which we obtained FIRE spectra are A 1 and A 2, which lie just outside and inside the 90% error circle, respectively. Whereas the spectrum of A 1 is featureless, the spectrum of A 2 clearly shows Br γ in emission (Figure 3). This H I emission feature is commonly associated with accreting sources (Bandyopadhyay et al. 1999, 2003), and its presence shows that A 2 is the true NIR counterpart of GX 3+1. Other H I, and possibly He I and He II, lines may be identified as well, but are much weaker; the $2.192 \mu\text{m}$ feature especially is very weak and may turn out not to be a real emission line in a higher signal-to-noise spectrum. Nevertheless, the spectrum of A 1 does not show similar features at the corresponding wavelengths. In Table 3, we list the measured wavelengths of the (tentative) emission lines. The equivalent width of the Br γ line is about $-45 \pm 5 \text{ \AA}$; given that the spectrum of A 2 still contains a small contribution from the light of A 1, the true value must be lower (i.e., more negative). No absorption features from a companion star can be seen in the spectrum of A 2 but we point out the poor signal-to-noise

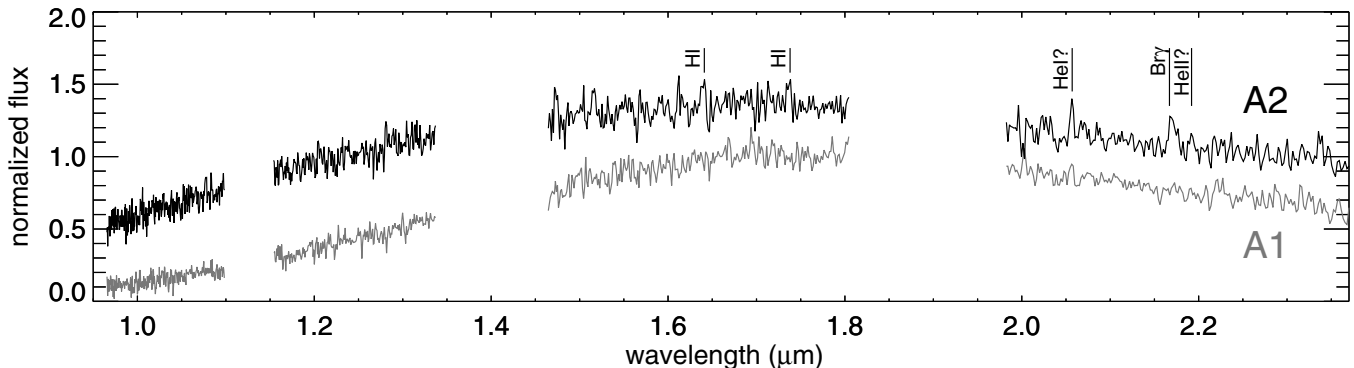


Figure 3. FIRE spectra of stars A 1 (bottom spectrum, gray) and A 2 (top, black). Emission lines of H I, and possibly He I and He II, that are (tentatively) identified in the spectrum of A 2 are marked. Sharp features in the spectrum, mostly apparent in the H band, result from imperfect sky subtraction. The spectra are normalized to the flux at $1.66 \mu\text{m}$ and an arbitrary offset of 0.3 flux units is applied to the spectrum of A 2 for clarity. Parts of the spectra where the transmission through the Earth's atmosphere is low are not plotted.

Table 3
Emission Lines in the spectrum of A 2

Line	λ_{obs} (μm)	λ_{vacuum} (μm)	Equivalent Width (\AA)
H I	1.641	1.642	-17 ± 3
H I	1.738	1.737	-13 ± 3
He I?	2.057	2.059	-13 ± 3
Br γ	2.167	2.166	-45 ± 5
He II?	2.192	2.189	-19 ± 3

Notes. Observed wavelengths λ_{obs} correspond to the locations of the peak flux values in the lines. Errors in the wavelengths are about $\pm 0.001 \mu\text{m}$. Due to the contamination by the light of A 1, the equivalent-width values are upper limits.

ratio especially in the H band (due to poor sky subtraction) and beyond $\sim 2.3 \mu\text{m}$, where the CO absorption bands appear as prominent features in the K -band spectra of stars of spectral type K and M.

We compare the magnitudes for star A 2 from epochs 2 and 3 to check for variability. Taking into account both the formal photometry errors from DAOPHOT and the photometric calibration errors, we do not see any sign of variability in K_s in excess of ~ 0.1 mag in our own observations (Table 2). The combined magnitudes of A 1 to A 4 are consistent with $K = 14.87 \pm 0.13$ mag for source A on 2007 May 3 as reported by Zolotukhin & Revnitsev (2011), and with $K = 15.13 \pm 0.16$ mag for that same source (i.e., star 311) on 1988 May 11–15 as reported by Naylor et al. (1991). This points to a lack of large-amplitude NIR variability on a timescale of years.

We also searched the Vista Variables in the Via Lactea (VVV) catalogs (Minniti et al. 2010) for detections of A 2. The most recent data release (DR), i.e., DR 3, has 18 images that cover the position of GX 3+1, including 10 epochs in the K_s band. However, in these images A 2 is not detected as a separate object but as a blend with, at least, A 1, or with A 1 and the bright object to the southwest of A 4 just outside of the 95% error circle (see Figure 2(c)). The poorer image quality of the VVV images compared to that of our images from epochs 2 and 3 is due partly to the coarser VVV pixel scale ($0''.34 \text{ pixel}^{-1}$) and partly to the seeing conditions under which these VVV images were taken ($\gtrsim 0''.8$). Reprocessing of the VVV images to attempt to extract deblended magnitudes for A 2 and A 1 is beyond the scope of this paper. A visual examination of the DR 3 images does not reveal any obvious brightness variations of A 2. The recently released multi-band master catalog extracted from the DR 1 images⁸ did not include a detection of A 2, either.

4. DISCUSSION AND CONCLUSIONS

The NIR emission from bright NS-LMXBs can originate in several parts of the system: the accretion disk may contribute via thermal emission that results from X-ray or viscous heating, a late-type secondary can produce thermal emission in the NIR, which may be enhanced by X-ray heating of the hemisphere facing the accretion region, and finally the inner region of a jet—if present—may contribute through optically thin synchrotron emission. *Spitzer* data of the NS-LMXB 4U 0614+091 suggest that one would have to observe at wavelengths $> 8 \mu\text{m}$ to detect emission from the optically thick part of the jet (Migliari

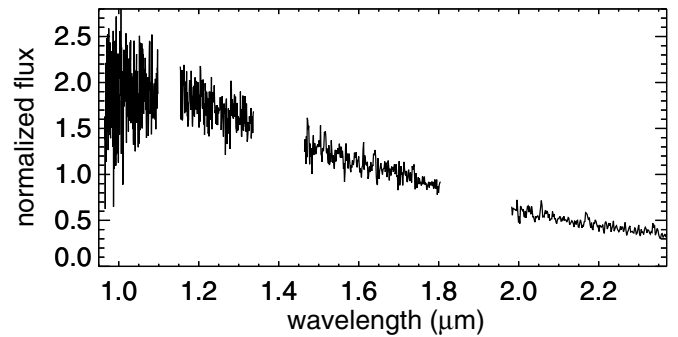


Figure 4. Dereddened spectrum of A 2 normalized to the flux at $1.66 \mu\text{m}$. We adopted $N_{\text{H}} = 1.59 \times 10^{22} \text{ cm}^{-2}$ following Oosterbroek et al. (2001) and assumed the extinction law from Cardelli et al. (1989). Adopting the extinction coefficients from Nishiyama et al. (2008) would result in a steeper continuum slope.

et al. 2010). For jets that are significantly stronger than the one in 4U 0614+091 the break between the optically thin and thick part of the jet may shift to shorter wavelengths (Falcke et al. 2004).

The FIRE spectrum of GX 3+1 indicates that at least a significant portion of the NIR light comes from a heated accretion disk or heated secondary. Both the emission lines and the blue (i.e., $F_{\nu} \propto \nu^{\alpha}$ with $\alpha > 0$) continuum of the unreddened spectrum (Figure 4) are as expected for a thermal component (Russell et al. 2007). Based on our NIR data alone, we are not able to distinguish between thermal disk emission resulting from either X-ray or viscous heating. This would require simultaneous NIR and X-ray observations to look for possible correlated behavior on timescales of seconds, as would be predicted by X-ray heating.

GX 3+1 has not been detected at radio wavelengths (Berendsen et al. 2000), suggesting there is no powerful jet in this system. Furthermore, optically thin synchrotron emission produces a red ($\alpha < 0$) NIR spectrum, which is clearly inconsistent with the spectrum in Figure 4. We note that the exact slope of the continuum is uncertain as contamination by the light from the close neighbor A 1 is not completely accounted for (see Section 2.2.3). However, in Figure 3, one can see that the observed spectrum of A 2 is bluer than that of A 1, thus, if anything, the effect of A 1 is to make the spectrum of A 2 seem redder. We conclude that most likely a jet does not significantly contribute to the NIR emission of GX 3+1.

To estimate the possible contribution of an unheated secondary, we first use the estimate of the column density toward GX 3+1 from Oosterbroek et al. (2001), viz. $N_{\text{H}} = 1.59^{+0.07}_{-0.12} \times 10^{22} \text{ cm}^{-2}$, and the distance of 6.1 kpc (with an estimated uncertainty of $\sim 15\%$; Kuulkers et al. 2003) to compute the absolute K_s magnitude of A 2. Adopting the relation $N_{\text{H}} = 1.79 \times 10^{21} A_{\text{V}} \text{ cm}^{-2}$ from Predehl & Schmitt (1995), $A_{\text{K}} = 0.114 \times A_{\text{V}}$ from Cardelli et al. (1989), and $A_{\text{K}} = 0.95 \times A_{\text{K}_s}$ from Dutra et al. (2002), we find $M_{\text{K}_s} = 0.84 \pm 0.35$, where the error is dominated by the uncertainty in the distance. However, since GX 3+1 lies close to the direction of the Galactic center, it may be more appropriate to adopt the conversion $A_{\text{K}_s} = 0.062 \times A_{\text{V}}$ from Nishiyama et al. (2008), which yields $M_{\text{K}_s} = 1.35 \pm 0.34$. We compare this value to the absolute K_s magnitudes of late-type dwarfs and giants, which typically are the donors in LMXBs. Main-sequence stars of spectral type G0 to M5 have $M_{\text{K}_s} = 3.0$ to 8.4 (Mamajek 2014.⁹) Therefore, if

⁸ http://www.eso.org/sci/observing/phase3/data_releases/VVV_CAT.2014-07-11.pdf

⁹ http://www.pas.rochester.edu/~emamajek/EEM_dwarf_UBVIJHK_colors_Teff.txt

the secondary is indeed a late-type dwarf, it does not provide a dominant ($>50\%$) contribution to the K_s flux. Giants of spectral type G0 and later have $M_{K_s} \lesssim -0.45$ (Ostlie & Carroll 2007; Bessell & Brett 1988) which is brighter than the bright limit to the estimated M_{K_s} for GX 3+1; therefore, we can exclude that the secondary is a late-type giant.

Given that the K_s flux from GX 3+1 is most likely thermal, we can estimate the orbital period, P_b , using M_{K_s} and the X-ray luminosity, L_X . A relation between these properties is expected if the NIR emission originates from thermal emission in the outer parts of the accretion disk (where X-ray reprocessing dominates over viscous heating), the size of which is set by the orbital separation of the binary stars—and thus the orbital period. van Paradijs & McClintock (1994) demonstrated the existence of such a correlation in the optical, and it has recently been extended to the NIR by Revnivtsev et al. (2012) based on a small sample of NS-LMXBs. For $L_X/L_{\text{Edd}} = 0.1\text{--}0.2$ and $M_{K_s} = 1.35 \pm 0.34$, we find that $P_b \approx 4.4\text{--}10.9$ hr using the equation in Section 4.2 in Revnivtsev et al. (2012)¹⁰; for $M_{K_s} = 0.84 \pm 0.35$, we find $P_b \approx 7.3\text{--}18.5$ hr. This range of periods also suggests that the secondary is not a giant (see, e.g., Verbunt 1993), though it leaves room for a somewhat evolved star or subgiant. Now that we have identified the NIR counterpart of GX 3+1, a targeted follow-up campaign of time-resolved spectroscopy or photometry may be attempted to directly measure the orbital period.

Russell et al. (2007) investigated the origin of the OIR emission in NS-LMXBs based on a set of near-simultaneous X-ray and OIR data. They found that both at luminosities below $L_X \approx 10^{36}$ erg s⁻¹ and at the high X-ray luminosity end (i.e., in the Z sources) most of the NIR emission comes from an X-ray-heated disk; for atolls and milli-second X-ray pulsars of intermediate luminosity, the jet emission dominates. The sample of NS-LMXBs studied by Russell et al. did not include the brightest atolls. In fact, NIR counterparts were discovered only recently for several of these systems, such as GX 9+1 (Curran et al. 2011), 4U 1705–44 (Homan et al. 2009), and now GX 3+1 (this work). The counterpart of GX 9+1 has not been studied in detail, yet. From JHK_s colors and correlations between near-simultaneous X-ray (3–100 keV) and K_s -band data, Homan et al. (2009) found that in 4U 1705–44, a source that can reach similar X-ray luminosities as GX 3+1, the NIR flux is likely the result of X-ray heating, like in the Z sources. They suggested that the high X-ray luminosity could be a sign of a larger disk compared to the disks in fainter atolls, which would explain the larger NIR contribution from X-ray heating. Our findings indicate that GX 3+1 behaves similarly to 4U 1705–44, in the sense that jet NIR emission does not play a (dominant) role; therefore, this scenario could offer a plausible explanation for the origin of the NIR emission in GX 3+1 as well.

Finally, we comment on the lack of variability of the NIR counterpart to GX 3+1. In Figure 1, the quasi-periodic modulations in the RXTE/ASM and MAXI count rate for GX 3+1 are clearly visible. If these brightness variations are truly the result of changes in the mass-accretion rate, it is expected that the NIR emission, which, as we show, contains a dominant contribution from an accretion disk or heated secondary, should also vary in time. For example, in the case of 4U 1705–44, Homan et al. (2009) clearly see correlated X-ray and NIR variations.

The difference in X-ray count rate between the epochs of our imaging observations is a factor of ~ 2 , but surprisingly, we see no change in the K_s magnitude within the photometric accuracy (~ 0.1 mag). We note that we only have good measurements of the NIR brightness at two epochs, and need further monitoring to investigate the (lack of) NIR variability of GX 3+1 in more detail.

The authors thank A. Monson for help with the FourStar data reduction and R. Remillard, P. Sullivan, and M. Matejek for obtaining part of the observations. This work is supported by *Chandra* grant GO2-13048X.

Facilities: CXO, RXTE, MAXI, Magellan:Baade (PANIC, FourStar, FIRE)

REFERENCES

- Bandyopadhyay, R. M., Shahbaz, T., & Charles, P. A. 2003, *MNRAS*, **340**, L13
- Bandyopadhyay, R. M., Shahbaz, T., Charles, P. A., & Naylor, T. 1999, *MNRAS*, **306**, 417
- Berendsen, S. G. H., Fender, R., Kuulkers, E., Heise, J., & van der Klis, M. 2000, *MNRAS*, **318**, 599
- Bertin, E. 2006, in ASP Conf. Ser. 351, *Astronomical Data Analysis Software and Systems XV*, ed. C. Gabriel et al. (San Francisco, CA: ASP), 112
- Bertin, E., Mellier, Y., Radovich, M., et al. 2002, in ASP Conf. Ser. 281, *Astronomical Data Analysis Software and Systems XI*, ed. D. A. Bohlender, D. Durand, & T. H. Handley (San Francisco, CA: ASP), 228
- Bessell, M. S., & Brett, J. M. 1988, *PASP*, **100**, 1134
- Bowyer, S., Byram, E. T., Chubb, T. A., & Friedman, H. 1965, *Sci*, **147**, 394
- Cardelli, J. A., Clayton, G. C., & Mathis, J. S. 1989, *ApJ*, **345**, 245
- Curran, P. A., Chaty, S., & Zurita Heras, J. A. 2011, *A&A*, **533**, A3
- den Hartog, P. R., in't Zand, J. J. M., Kuulkers, E., et al. 2003, *A&A*, **400**, 633
- Durant, M., Cornelisse, R., Remillard, R., & Levine, A. 2010, *MNRAS*, **401**, 355
- Dutra, C. M., Santiago, B. X., & Bica, E. 2002, *A&A*, **381**, 219
- Falcke, H., K rding, E., & Markoff, S. 2004, *A&A*, **414**, 895
- Fruscione, A., McDowell, J. C., Allen, G. E., et al. 2006, *Proc. SPIE*, **6270**, 1
- Gilfanov, M. 2004, *MNRAS*, **349**, 146
- Hasinger, G., & van der Klis, M. 1989, *A&A*, **225**, 79
- Homan, J., Kaplan, D. L., van den Berg, M., & Young, A. J. 2009, *ApJ*, **692**, 73
- Homan, J., van der Klis, M., Fridriksson, J. K., et al. 2010, *ApJ*, **719**, 201
- Home, K. 1986, *PASP*, **98**, 609
- Kotze, M. M., & Charles, P. A. 2010, *MNRAS*, **402**, L16
- Kuulkers, E., den Hartog, P. R., in't Zand, J. J. M., et al. 2003, *A&A*, **399**, 663
- Kuulkers, E., & van der Klis, M. 2000, *A&A*, **356**, L45
- Levine, A. M., Bradt, H., Cui, W., et al. 1996, *ApJL*, **469**, L33
- Makishima, K., Mitsuda, K., Inoue, H., et al. 1983, *ApJ*, **267**, 310
- Martini, P., Persson, S. E., Murphy, D. C., et al. 2004, *Proc. SPIE*, **5492**, 1653
- Matsuoka, M., Kawasaki, K., Ueno, S., et al. 2009, *PASJ*, **61**, 999
- Migliari, S., Tomsick, J. A., Miller-Jones, J. C. A., et al. 2010, *ApJ*, **710**, 117
- Minniti, D., Lucas, P. W., Emerson, J. P., et al. 2010, *NewA*, **15**, 433
- Monson, A., Persson, E., Murphy, D., Birk, C., & Kelson, D. 2011, *FourStar Manual* (http://instrumentation.obs.carnegiescience.edu/FourStar/Documents/FourStar_Documentation.pdf)
- Naylor, T., Charles, P. A., & Longmore, A. J. 1991, *MNRAS*, **252**, 203
- Nishiyama, S., Nagata, T., Tamura, M., et al. 2008, *ApJ*, **680**, 1174
- Oosterbroek, T., Barret, D., Guainazzi, M., & Ford, E. C. 2001, *A&A*, **366**, 138
- Ostlie, D., & Carroll, B. 2007, *An introduction to Modern Stellar Astrophysics* (2nd ed.; Reading, MA: Addison-Wesley)
- Predehl, P., & Schmitt, J. H. M. M. 1995, *A&A*, **293**, 889
- Revnivtsev, M., Postnov, K., Kuranov, A., & Ritter, H. 2011, *A&A*, **526**, A94
- Revnivtsev, M. G., Zolotukhin, I. Y., & Meshcheryakov, A. V. 2012, *MNRAS*, **421**, 2846
- Russell, D. M., Fender, R. P., & Jonker, P. G. 2007, *MNRAS*, **379**, 1108
- Simcoe, R. A., Burgasser, A. J., Schechter, P. L., et al. 2013, *PASP*, **125**, 270
- Taam, R. E. 1983, *ApJ*, **270**, 694
- Vacca, W. D., Cushing, M. C., & Rayner, J. T. 2003, *PASP*, **115**, 389
- van Paradijs, J., & McClintock, J. E. 1994, *A&A*, **290**, 133
- Verbunt, F. 1993, *ARA&A*, **31**, 93
- Webbink, R. F., Rappaport, S., & Savonije, G. J. 1983, *ApJ*, **270**, 678
- Zolotukhin, I. Y., & Revnivtsev, M. G. 2011, *MNRAS*, **411**, 620
- Zombeck, M. V., Chappell, J. H., Kenter, A. T., et al. 1995, *Proc. SPIE*, **2518**, 96

¹⁰ Revnivtsev et al. (2012) use the 2–10 keV luminosity rather than the bolometric luminosity, which is why the adopted L_X/L_{Edd} range is 0.1–0.2 (reflecting the $(2\text{--}4) \times 10^{37}$ erg s⁻¹ range found by den Hartog et al. 2003; see Section 1) rather than 0.15–0.3.